Computation of the intensities of parametric holographic scattering patterns in photorefractive crystals

Simon Schwalenberg*
Fachbereich Physik, Universität Osnabrück, Barbarastrasse 7, 49069 Osnabrück, Germany
(Received 25 February 2005; published 21 June 2005)

The present work represents a first attempt to perform computations of output intensity distributions for different parametric holographic scattering patterns. Based on the model for parametric four-wave mixing processes in photorefractive crystals and taking into account realistic material properties, we present computed images of selected scattering patterns. We compare these calculated light distributions to the corresponding experimental observations. Our analysis is especially devoted to dark scattering patterns as they make high demands on the underlying model.

DOI: 10.1103/PhysRevE.71.066608 PACS number(s): 42.70.Nq, 78.20.Bh

I. INTRODUCTION

Holographic scattering in electro-optic crystals originates from light-induced refractive index changes [1]. Incident light waves (pump waves) and waves scattered from volume or surface imperfections of the crystal (seed scattering) record "noisy" volume phase gratings. Subsequently, the initial scattering waves may be amplified or attenuated by the pump waves due to direct coupling of two waves via a shifted grating [2] or because of parametric mixing [3,4] of more than two waves via several gratings. A special class of holographic scattering processes is based on parametric four-wave mixing, where two pump waves and two scattering waves are involved. A comprehensive theory to describe these parametric processes in photorefractive media has been developed by Sturman *et al.* [5]. Many parametric holographic scattering processes have been investigated by studying exponential gain factors for the initial scattering light. The model [5], however, provides the opportunity for a detailed theoretical investigation of scattering light intensities. This is especially interesting for parametric processes which are not dominated by strong exponential amplification—e.g., weak and dark scattering patterns.

Based on the model of [5], it is the aim of the present work to calculate and visualize the intensity distribution of parametric scattering patterns. Numerical simulations have previously been performed for the propagation of a light beam (including beam fanning) in a photorefractive medium [6,7]. We devote our computations to the parametric four-wave mixing processes which are responsible for the recently observed dark scattering patterns in photorefractive strontium-barium-niobate (SBN) [8] and barium-calcium-titante (BCT) [9] crystals. The computed scattered light images are compared qualitatively to photographs of the corresponding experimental observations. Additionally, we give a theoretical explanation of the process which forms the so-called inner scattering cone (ring) in lithium-niobate ($LiNbO_3$). This scattering cone has been discovered in experiments with only one pump beam for different materials [10–12]. In the case of $LiNbO_3$:Fe [11] the observation of a dark ring on the bright scattering background has been reported, but not explained so far.

II. SETUP OF PARAMETRIC HOLOGRAPHIC SCATTERING EXPERIMENTS

The experimental configuration used for the investigation of parametric scattering processes is illustrated in Fig. 1. Additionally, the figure shows a photograph of a typical light distribution on a screen behind a BCT crystal. The sample is illuminated symmetrically by two laser/pump beams (here of extraordinary polarization) with the wavelength λ. They intersect at an angle of $2\theta_p$ (in air) in the plane of incidence which in this configuration is perpendicular to the *c* axis of the crystal. A polarization film (analyzer) behind the sample may be used to adjust the intensity ratio of the isotropically diffracted light (polarization conserved) and the anisotropically diffracted light (polarization changed).

III. MATHEMATICAL FORMULATION OF THE MODEL

For the computation of the intensities of parametric four-wave mixing processes in photorefractive crystals, we strictly follow the theoretical description introduced in [5]. Parametric scattering processes are fundamentally divided into $\mathcal{A}$ and $\mathcal{B}$ processes, which are observed as rings and

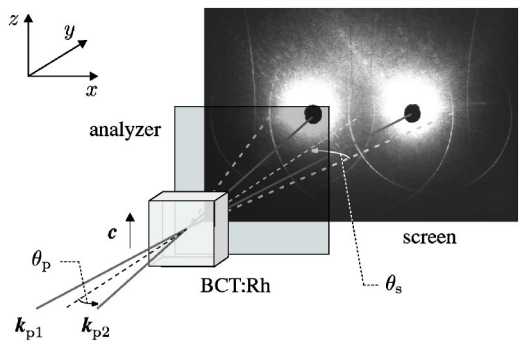

FIG. 1. Sketch of the experimental arrangement used for the investigation of parametric holographic scattering patterns.

*Electronic address: Simon.Schwalenberg@uos.de

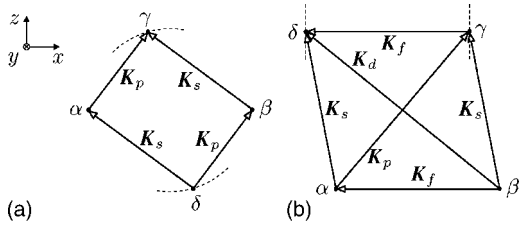

FIG. 2. Schematic diagrams of the grating vectors involved in an $\mathcal{A}$ process (a) and $\mathcal{B}$ process (b). The positions α, β, γ, and δ mark the tips of the corresponding wave vectors.

lines, respectively, on a screen behind the crystal (see Fig. 1). The waves involved in an $\mathcal{A}$ process fulfill the phase-matching condition

$$\boldsymbol{k}_\alpha^p + \boldsymbol{k}_\beta^q = \boldsymbol{k}_\gamma^r + \boldsymbol{k}_\delta^s, \tag{1a}$$

while $\mathcal{B}$ processes are connected to the phase-matching condition

$$\boldsymbol{k}_\alpha^p - \boldsymbol{k}_\beta^q = \boldsymbol{k}_\gamma^r - \boldsymbol{k}_\delta^s. \tag{1b}$$

Here $\boldsymbol{k}_\alpha$ and $\boldsymbol{k}_\beta$ are the wave vectors of the pump waves α and β, while $\boldsymbol{k}_\gamma$ and $\boldsymbol{k}_\delta$ are the wave vectors of the scattering waves γ and δ. The superscripts $p,q,r,s \in \{\mathrm{o},\mathrm{e}\}$ entering Eqs. (1a) and (1b) denote the polarization (ordinary, extraordinary) of the four involved waves. In uniaxial crystals this leads to 19 elementary scattering processes which are written in the compact notation $\mathcal{T}:(pq-rs)$ with $\mathcal{T} \in \{\mathcal{A},\mathcal{B}\}$ as the process type. The grating vectors involved in an $\mathcal{A}$ and $\mathcal{B}$ process are defined as shown in Figs. 2(a) and 2(b), respectively. For an $\mathcal{A}$ process they are given by

$$\begin{aligned} \boldsymbol{K}_s &= \boldsymbol{k}_\gamma - \boldsymbol{k}_\delta \equiv \boldsymbol{k}_\alpha - \boldsymbol{k}_\delta, \\ \boldsymbol{K}_p &= \boldsymbol{k}_\gamma - \boldsymbol{k}_\alpha \equiv \boldsymbol{k}_\beta - \boldsymbol{k}_\delta, \end{aligned} \tag{2a}$$

and for a $\mathcal{B}$ process by

$$\begin{aligned} \boldsymbol{K}_s &= \boldsymbol{k}_\gamma - \boldsymbol{k}_\delta \equiv \boldsymbol{k}_\delta - \boldsymbol{k}_\alpha, \\ \boldsymbol{K}_f &= \boldsymbol{k}_\alpha - \boldsymbol{k}_\beta \equiv \boldsymbol{k}_\delta - \boldsymbol{k}_\gamma, \\ \boldsymbol{K}_p &= \boldsymbol{k}_\gamma - \boldsymbol{k}_\alpha, \\ \boldsymbol{K}_d &= \boldsymbol{k}_\delta - \boldsymbol{k}_\beta. \end{aligned} \tag{2b}$$

The phase-matching conditions (1a) and (1b) determine the angular distribution of the scattering patterns. This distribution depends on the wavelength λ and the refractive indices for ordinary and extraordinary polarization n_o and n_e. Furthermore, each parametric scattering pattern has a characteristic dependence of the apex angle θ on the pump angle θ_p (see Fig. 1) which allows us to identify the scattering pattern with a certain four-wave mixing process.

For the computation of the steady-state intensities of scattering patterns it is necessary to study the coupling of the four involved waves α, β, γ, and δ. We represent these waves in the form

$$\boldsymbol{\mathcal{E}} = A\boldsymbol{e}\exp\{i(\boldsymbol{k}\cdot\boldsymbol{r} - \omega t)\} \quad \text{with} \quad A = \overline{A}\exp\{i\Phi\}. \tag{3}$$

Here $\boldsymbol{e}$ is the unit polarization vector and A is the complex amplitude composed of the absolute value $\overline{A}$ and the phase Φ. Furthermore, $\boldsymbol{k}$ is the wave vector and ω the frequency of the wave. The interaction of light waves in photorefractive media can be described by the coupled-wave equations (in the one-dimensional case)

$$\begin{pmatrix} \partial/\partial y \\ \partial/\partial y \end{pmatrix} \begin{pmatrix} A_\gamma \\ A_\delta^* \end{pmatrix} = \begin{pmatrix} V_{\gamma\gamma} & V_{\gamma\delta} \\ V_{\delta\gamma} & V_{\delta\delta} \end{pmatrix} \begin{pmatrix} A_\gamma \\ A_\delta^* \end{pmatrix} \tag{4a}$$

for an $\mathcal{A}$ process and

$$\begin{pmatrix} \partial/\partial y \\ \partial/\partial y \end{pmatrix} \begin{pmatrix} A_\gamma \\ A_\delta \end{pmatrix} = \begin{pmatrix} U_{\gamma\gamma} & U_{\gamma\delta} \\ U_{\delta\gamma} & U_{\delta\delta} \end{pmatrix} \begin{pmatrix} A_\gamma \\ A_\delta \end{pmatrix} \tag{4b}$$

for an $\mathcal{B}$ process. Here A_γ and A_δ are the (complex) amplitudes of the scattering waves γ and δ. The asterisk denotes complex conjugation. Within the undepleted pump approximation the amplitudes A_α and A_β of the pump waves α and β are considered constant with respect to the operator for spatial differentiation $\partial/\partial y$. Finally, V_{jk} and U_{jk} are the elements of the interaction matrix for an $\mathcal{A}$ and $\mathcal{B}$ process, which describe the coupling of the four involved waves as explained later. Neglecting angular detunings, the system of equations (4b) for the $\mathcal{B}$ process has the explicit solution

$$\begin{aligned} A_\gamma = &\left[\frac{A_\gamma^0}{2}\left(1 + \frac{U_{\gamma\gamma} - U_{\delta\delta}}{\Gamma_+ - \Gamma_-}\right) + \frac{A_\delta^0 U_{\gamma\delta}}{\Gamma_+ - \Gamma_-}\right]\exp(\Gamma_+ y) \\ &+ \left[\frac{A_\gamma^0}{2}\left(1 - \frac{U_{\gamma\gamma} - U_{\delta\delta}}{\Gamma_+ - \Gamma_-}\right) + \frac{A_\delta^0 U_{\gamma\delta}}{\Gamma_+ - \Gamma_-}\right]\exp(\Gamma_- y), \end{aligned} \tag{5}$$

$$\begin{aligned} A_\delta = &\left[\frac{A_\delta^0}{2}\left(1 + \frac{U_{\delta\delta} - U_{\gamma\gamma}}{\Gamma_+ - \Gamma_-}\right) + \frac{A_\gamma^0 U_{\delta\gamma}}{\Gamma_+ - \Gamma_-}\right]\exp(\Gamma_+ y) \\ &+ \left[\frac{A_\delta^0}{2}\left(1 - \frac{U_{\delta\delta} - U_{\gamma\gamma}}{\Gamma_+ - \Gamma_-}\right) - \frac{A_\gamma^0 U_{\delta\gamma}}{\Gamma_+ - \Gamma_-}\right]\exp(\Gamma_- y). \end{aligned} \tag{6}$$

The solution for the $\mathcal{A}$ process can be obtained easily by the substitution $U \to V$ and $A_\delta \to A_\delta^*$. Here $A_{\gamma,\delta}^0$ are the initial amplitudes of the scattering waves γ and δ at the input crystal plane ($y=0$). Furthermore, Γ_+ and Γ_- are the characteristic complex gain coefficients

$$\Gamma_\pm = \frac{1}{2}[V_{\gamma\gamma} + V_{\delta\delta} \pm \sqrt{(V_{\gamma\gamma} - V_{\delta\delta})^2 + 4V_{\gamma\delta}V_{\delta\gamma}}], \tag{7a}$$

$$\Gamma_\pm = \frac{1}{2}[U_{\gamma\gamma} + U_{\delta\delta} \pm \sqrt{(U_{\gamma\gamma} - U_{\delta\delta})^2 + 4U_{\gamma\delta}U_{\delta\gamma}}], \tag{7b}$$

for $\mathcal{A}$ and $\mathcal{B}$ processes, respectively. In order to calculate the intensities $I_{\gamma,\delta} = |A_{\gamma,\delta}|^2$ at the back face of the crystal ($y=d$), we have to find expressions for the elements of the interaction matrices $\hat{V}$ and $\hat{U}$. According to [5] they are defined as

$$V_{\gamma\gamma} = -i\kappa[I_\alpha\langle\gamma,\alpha|\hat{r}|p\rangle\langle p|\hat{E}|\gamma,\alpha\rangle + I_\beta\langle\gamma,\beta|\hat{r}|s\rangle\langle s|\hat{E}|\gamma,\beta\rangle],$$

$$V_{\delta\delta} = i\kappa[I_\alpha\langle\alpha,\delta|\hat{r}|s\rangle\langle s|\hat{E}|\alpha,\delta\rangle + I_\beta\langle\beta,\delta|\hat{r}|p\rangle\langle p|\hat{E}|\beta,\delta\rangle],$$

$$V_{\gamma\delta} = -i\kappa[\langle\gamma,\beta|\hat{r}|s\rangle\langle s|\hat{E}|\alpha,\delta\rangle + \langle\alpha,\gamma|\hat{r}|p\rangle\langle p|\hat{E}|\beta,\delta\rangle]A_\alpha A_\beta,$$

$$V_{\delta\gamma} = i\kappa[\langle\beta,\delta|\hat{r}|p\rangle\langle p|\hat{E}|\gamma,\alpha\rangle + \langle\alpha,\delta|\hat{r}|s\rangle\langle s|\hat{E}|\gamma,\beta\rangle]A_\alpha^* A_\beta^*, \tag{8a}$$

for an $\mathcal{A}$ process, and

$$U_{\gamma\gamma} = -i\kappa[I_\alpha\langle\gamma,\alpha|\hat{r}|p\rangle\langle p|\hat{E}|\gamma,\alpha\rangle + I_\beta\langle\gamma,\beta|\hat{r}|s\rangle\langle s|\hat{E}|\gamma,\beta\rangle],$$

$$U_{\delta\delta} = -i\kappa[I_\alpha\langle\delta,\alpha|\hat{r}|s\rangle\langle s|\hat{E}|\delta,\alpha\rangle + I_\beta\langle\delta,\beta|\hat{r}|d\rangle\langle d|\hat{E}|\delta,\beta\rangle],$$

$$U_{\gamma\delta} = -i\kappa[\langle\gamma,\beta|\hat{r}|s\rangle\langle s|\hat{E}|\delta,\alpha\rangle + \langle\delta,\gamma|\hat{r}|f\rangle\langle f|\hat{E}|\alpha,\beta\rangle^*]A_\alpha^* A_\beta,$$

$$U_{\delta\gamma} = -i\kappa[\langle\delta,\alpha|\hat{r}|s\rangle\langle s|\hat{E}|\gamma,\beta\rangle + \langle\delta,\gamma|\hat{r}|f\rangle\langle f|\hat{E}|\alpha,\beta\rangle]A_\alpha A_\beta^*, \tag{8b}$$

for a $\mathcal{B}$ process, with $\kappa=\pi n^3/\lambda$ and $I_{\alpha,\beta}=|A_{\alpha,\beta}|^2$. The variables p, s, d, and f indicate the involved gratings (2a) and (2b). Each matrix element of Eqs. (8a) and (8b) is composed of products of two fundamental quantities: the $\hat{E}$ factor and the $\hat{r}$ factor. These two terms allow us to resolve the full parametric scattering process into single recording and readout processes, respectively. The $\hat{r}$ factor is a measure for the efficiency of a single diffraction/readout process for a pair of waves μ and ρ coupled via a recorded grating ν:

$$\langle\mu,\rho|\hat{r}|\nu\rangle = e_i^\mu e_j^\rho r_{ijk}\nu_k, \tag{9}$$

with $\boldsymbol{e}^\mu$ and $\boldsymbol{e}^\rho$ as the unit polarization vectors of the coupled waves μ and ρ, r_{ijk} as the elements of the linear electro-optic tensor, and $\boldsymbol{\nu}=\boldsymbol{K}^\nu/|\boldsymbol{K}^\nu|$ as the involved unit grating vector. Each $\hat{r}$ factor entering Eqs. (8a) and (8b) is combined with the $\hat{E}$ factor which includes the properties related to the recording mechanism of the corresponding grating/space-charge field. For our computation of the intensities of parametric four-wave mixing processes in photorefractive crystals, we substantially apply the isotropic model of [5] which includes the assumption that the (specific) photoconductivity $\alpha\chi$, the dielectric permittivity ε, and the light absorption α are scalar parameters. We take into account space-charge-field-limiting effects resulting from a finite effective trap density N_{eff}. In our computations we want to focus on the elementary parametric scattering processes without an external electric field. Then the $\hat{E}$ factor for a grating ν recorded by the waves μ and ρ is given by the relation

$$\langle\nu|\hat{E}|\mu,\rho\rangle = -\frac{(i\overline{\sigma}E_{\text{D}}^\nu D_{\text{s}}^\nu)(\boldsymbol{e}^\mu\cdot\boldsymbol{e}^\rho) + (\alpha\chi)^{-1}\langle\nu|\hat{\beta}|\mu,\rho\rangle}{I_0(1-i\Omega^\nu t_{\text{d}})}. \tag{10}$$

Here $E_{\text{D}}^\nu = K^\nu k_{\text{B}}T/e$ is the diffusion field and $\overline{\sigma}$ the electron-hole competition factor, which is 1 for pure electron and -1 for pure hole transport. The quantity $D_{\text{s}}^\nu=(1+K_\nu^2 r_{\text{d}}^2)^{-1}$ contains the effect of spatial screening with $r_{\text{d}}=(\varepsilon\varepsilon_0 k_{\text{B}}T/eN_{\text{eff}})^{1/2}$ as the Debye screening length, T as the temperature, and k_{B} as the Boltzmann constant. The anisotropy of the dielectric tensor may be included additionally by interpreting ε as the effective value $\varepsilon=\boldsymbol{\nu}\hat{\varepsilon}\boldsymbol{\nu}$ in the direction of the (unit) grating vector $\boldsymbol{\nu}$. The quantity $I_0=I_\alpha+I_\beta$ is the overall intensity, t_{d} is the dielectric relaxation time, and $\Omega^\nu=\omega_\mu-\omega_\rho$ is the frequency detuning of the recording waves μ and ρ. The photovoltaic charge transport is included in the $\hat{\beta}$ factor:

$$\langle\nu|\hat{\beta}|\mu,\rho\rangle = \beta_{imn}\nu_i e_m^\mu e_n^\rho. \tag{11}$$

Here β_{imn} are the elements of the (complex) photovoltaic tensor which may be represented in the form $\beta=\beta^{\text{s}}+i\beta^{\text{a}}$ with real numbers β^{s} and β^{a}.

The structure of the interaction matrices (8a) and (8b) allows us to investigate the involved energy transfer mechanisms individually. The diagonal elements $V_{\gamma\gamma}$, $V_{\delta\delta}$, and $U_{\gamma\gamma}$, $U_{\delta\delta}$ describe the contribution of direct two-wave mixing (2WM) to the energy transfer, irrespective of the phase-matching conditions (1a) and (1b). Here the scattering waves are coupled with the pump waves via gratings recorded by the coupled waves themselves. As a consequence these diagonal elements are responsible for the wide-angle scattering background. The nondiagonal elements $V_{\gamma\delta}$, $V_{\delta\gamma}$ and $U_{\gamma\delta}$, $U_{\delta\gamma}$ describe the contribution of true four-wave mixing (4WM), which in this model can be nonzero only in the case of exact phase matching. Here a pair of waves are coupled via a grating recorded by a different pair of waves. In contrast to the scattering background, the intensity of parametric scattering patterns stems from both the 2WM and 4WM parts.

IV. APPLICATION OF THE MODEL

A. Coordinates

The wave vectors of the pump and scattering waves are described in spherical coordinates θ and ϕ:

$$\boldsymbol{k}_\alpha = k_0 n_\alpha \begin{pmatrix} \sin\theta_{\text{p}} \\ \cos\theta_{\text{p}} \\ 0 \end{pmatrix}, \tag{12}$$

$$\boldsymbol{k}_\beta = k_0 n_\beta \begin{pmatrix} -\sin\theta_{\text{p}} \\ \cos\theta_{\text{p}} \\ 0 \end{pmatrix}, \tag{13}$$

$$\boldsymbol{k}_\gamma = k_0 n_\gamma \begin{pmatrix} \sin\theta_\gamma\cos\phi_\gamma \\ \cos\theta_\gamma \\ \sin\theta_\gamma\sin\phi_\gamma \end{pmatrix}, \tag{14}$$

$$\boldsymbol{k}_\delta = k_0 n_\delta \begin{pmatrix} \sin\theta_\delta\cos\phi_\delta \\ \cos\theta_\delta \\ \sin\theta_\delta\sin\phi_\delta \end{pmatrix}. \tag{15}$$

Here $k_0=2\pi/\lambda$ with λ as the (vacuum) wavelength. Furthermore, θ is the polar angle (from the y axis) and ϕ the azimuth angle (in the xz plane). The meaning of θ and ϕ is illustrated in Fig. 3.

The quantities n_α, n_β, n_γ, and n_δ are the refractive indices of the corresponding waves. For the investigation of intensi-

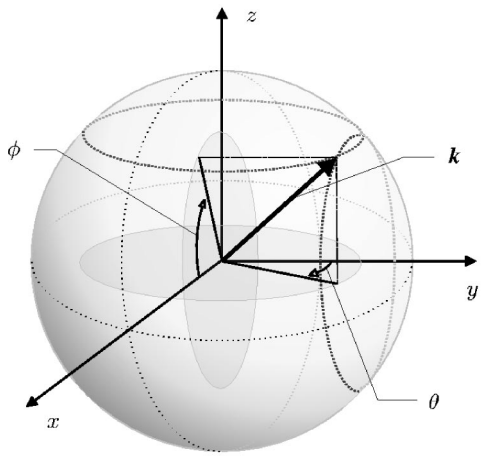

FIG. 3. Illustration of the spherical coordinates θ and ϕ to describe the orientation of the wave vector k.

ties, we may consider n_e as constant with respect to the azimuth angle ϕ. In the case of exact phase matching, the spherical coordinates θ and ϕ allow us to describe the position of parametric scattering patterns in three-dimensional space. For the special point at $\phi_{\gamma,\delta}=0°$ (xy plane), the corresponding apex angles $\theta_{\gamma,\delta}$ can be calculated for all 19 elementary scattering processes in uniaxial crystals by the relations given in [5]. The position in the three-dimensional space can be obtained by substituting the wave vectors (12)–(15) into the phase-matching conditions (1a) and (1b). For each type of process, this yields three equations (due to three spatial dimensions) in the four variables $\phi_\gamma, \theta_\gamma$ and $\phi_\delta, \theta_\delta$. Additional parameters are the pump angle θ_p (here inside the crystal), the refractive indices (corresponding to the polarizations), and the wavelength λ, which can be chosen according to a certain material and experimental configuration. In contrast, the azimuth angle ϕ_γ of the scattering wave γ can be regarded as a free parameter ranging from 0° to 360°. To each value of ϕ_γ the phase-matching condition determines the corresponding apex angle θ_γ as well as the angles ϕ_γ and ϕ_δ of the scattering wave δ. This also determines the involved grating vectors which are required to calculate the elements of the interaction matrices (8a) and (8b). Finally, we transform the spherical coordinates θ and ϕ inside the sample into Cartesian coordinates x and z in air which correspond to the position of the waves on the screen behind the crystal. Here we have to take into account the distance between the crystal and screen and Snellius' law due to refraction on the back face of the crystal.

The polarization vectors entering the $\hat{r}$, $\hat{E}$, and $\hat{\beta}$ factors (9)–(11) are approximated by

$$\boldsymbol{e}_o = \begin{pmatrix} 1 \\ 0 \\ 0 \end{pmatrix}, \quad \boldsymbol{e}_e = \begin{pmatrix} 0 \\ 0 \\ 1 \end{pmatrix}, \tag{16}$$

for ordinary and extraordinary polarized light, respectively.

B. Initial scattering waves: Amplitudes and phases

The steady-state amplitudes (5) and (6) of the scattering waves γ and δ depend on the (complex) initial amplitudes of all four involved waves, which contain information about the absolute values $\overline{A^0_\alpha}$, $\overline{A^0_\beta}$, $\overline{A^0_\gamma}$, and $\overline{A^0_\delta}$ of the amplitudes and the initial phases Φ^0_α, Φ^0_β, Φ^0_γ, and Φ^0_δ.

The absolute values can be extracted from the corresponding intensities by the relation $I=|A|^2$. The intensities I_α and I_β of the two pump beams are parameters known from the experiment. The intensities of the initial scattering waves, however, depend on many crystal properties. The mechanism which forms the seed scattering distribution $I^0(x,z)$ is complex and not yet fully understood. For our calculations we assume that, in general, each pump beam ρ induces a radial-symmetric seed scattering intensity distribution $I^0_\rho(x,z) \rightarrow I^0_\rho(\vartheta)$. Here the intensity of the seed scattering waves only depends on the angle ϑ^{out} (measured outside the crystal in rad) they form with the corresponding pump wave:

$$I^0_\rho(\vartheta^{out}) = I^i_{max} \exp\{-\vartheta^{out}/m\} + I^a_{max} \exp\{-\vartheta^{out}/m\}. \tag{17}$$

The quantity I^i_{max} is the maximum intensity of the isotropic initial scattering for $\vartheta^{out} \rightarrow 0°$ and I^a_{max} the corresponding anisotropic contribution. The expression $I^i_{max} \exp\{-\vartheta^{out}/m\}$ entering Eq. (17) is an approximation to the results for the angular distribution of the isotropic seed scattering along the c axis determined for SBN:Ce [13]. The parameters of our approximation are $m=0.22$ and I^i_{max} which is approximately 4.4×10^{-5} times the intensity of the corresponding pump beam. The anisotropic part of the initial scattering is assumed to be one order of magnitude lower than the isotropic part ($I^a_{max}/I^i_{max} \approx 0.1$). Finally, the overall initial scattering distribution $I^0(\vartheta)$ used in our calculations is a superposition of the two radial-symmetric distributions (17), one for each pump beam. The seed scattering approximation presented in this section is used for all crystals included in the present work. We do not take into account further crystal-specific influences as they differ even for samples of the same material.

The initial phases Φ^0_α, Φ^0_β, Φ^0_γ, and Φ^0_δ of the waves also effect the steady-state amplitudes (5) and (6) implicitly via the preexponential factors, while, in contrast, the exponential gain factors are independent of the initial phases. As a result, the intensity of the scattering waves is modulated by a characteristic function Π composed of the four initial phases Φ^0_α, Φ^0_β, Φ^0_γ, and Φ^0_δ. This feature has not yet been investigated experimentally; therefore, we do not study this dependence in the context of the present work. In our calculations we chose exemplary values for the initial phases, which correspond to the maximum of Π (optimal case yielding highest output intensities). These values may change for different scattering processes.

C. Frequency detunings

Frequency detunings due to temporal fluctuations of the pump intensity and space-charge field also have an effect on the scattering amplitudes via the $\hat{E}$ factor (10). For our computations it is necessary to know the frequencies of all four involved waves. If we assume equal frequencies of the pump waves ($\omega_\alpha=\omega_\beta$), then we can describe the frequency shift of an arbitrary scattering wave μ by $\Omega_\mu=\omega_\mu-\omega_\alpha$. Generally, we have to assume that the frequency shifts differ both in

absolute value and in the sign. For the scattering waves γ and δ involved in a parametric process, however, the frequency detunings are restricted according to the relations

$$\omega_\alpha + \omega_\beta = \omega_\gamma + \omega_\delta, \tag{18a}$$

$$\omega_\alpha - \omega_\beta = \omega_\gamma - \omega_\delta, \tag{18b}$$

for $\mathcal{A}$ and $\mathcal{B}$ processes, respectively. According to our assumption $\omega_\alpha = \omega_\beta$, Eqs. (18a) and (18b) lead to the following conditions for the frequency shifts of the scattering waves: $\Omega_\gamma = -\Omega_\delta$ for an $\mathcal{A}$ process and $\Omega_\gamma = \Omega_\delta$ for a $\mathcal{B}$ process. As a consequence we can express the frequencies ω_γ and ω_δ of the scattering waves in the form

$$\omega_\gamma = \omega_\alpha \pm \Omega, \quad \omega_\delta = \omega_\alpha \mp \Omega, \tag{19a}$$

$$\omega_\gamma = \omega_\alpha \pm \Omega, \quad \omega_\delta = \omega_\alpha \pm \Omega, \tag{19b}$$

for $\mathcal{A}$ and $\mathcal{B}$ processes, respectively. Here Ω is a parameter introduced to describe the absolute value of a frequency shift assumed for a certain process. As indicated by the "$\pm$" sign, we have two independent pairs $(\omega_\gamma, \omega_\delta)$ and $(\tilde{\omega}_\gamma, \tilde{\omega}_\delta)$ of detuned frequencies for each process. In the framework of our computations of parametric holographic scattering processes, we present only results for the pair which leads to the highest output intensities of the scattering waves.

D. Experimental and material-specific parameters

Computations of the intensities of parametric four-wave mixing processes are performed with the following experimental constants: We use pump light of the wavelength $\lambda = 532$ nm which corresponds to the experiments of [8,9]. The intensities of the pump beams are set to be $I_\alpha = I_\beta = 300$ mW cm^{-2}. Furthermore, the temperature entering the diffusion field is set to $T = 300$ K (room temperature). We do not include external electric fields. The material-specific parameters and properties required for our calculations are listed in Tables I–III. In detail, Tables I and II correspond to the materials SBN:Cr and BCT:Rh, respectively, as used in the experiments of [8,9]. For these materials we do not take into account the photovoltaic effect. Table III shows typical values of a highly doped $LiNbO_3$:Fe crystal. We want to note that the numbers listed in Tables I–III are considered to be an example of realistic initial parameters for the corresponding materials. We do not want to discuss the suitability and accuracy of the properties in the present work.

V. INTENSITY DISTRIBUTIONS AND DISCUSSION

In this section we present the results of our computations of selected parametric scattering patterns. The calculated intensities will be presented in the form of a computed image of the screen, rendered in a size of 400×400 pixels. Each pixel contains the intensity of the ordinary and extraordinary light (stored separately). First the image is initialized with the seed scattering distribution as defined in Sec. IV B. In a second step we calculate the wide-angle polarization isotropic and anisotropic scattering background for the full size of the image, irrespective of any phase-matching condition. In this context, only the 2WM contributions are involved. The intensity of the pixels which are located on the scattering pattern will be calculated by taking into account both the 2WM and 4WM contributions—e.g., the diagonal and nondiagonal elements of the interaction matrices. Additionally to the computed image, we present the intensity of the scattering wave along a particular pattern in a two-dimensional plot of the intensity versus the azimuth angle ϕ (as introduced in Sec. IV A).

TABLE I. Set of material-specific parameters needed for the computation of parametric scattering processes in the SBN:Cr sample used in [8]. The effective trap density has been determined for a similar SBN crystal doped with 0.02 wt % Cr.

Property	Value	Ref.
Material	$Sr_{0.61}Ba_{0.39}Nb_2O_6$	
Doping	0.046 wt % Cr	
Symmetry group	4*mm*	
Refractive indices	$n_o = 2.358$, $n_e = 2.325$	[14]
	$r_{13} = r_{23} = 56$ pm/V,	[15]
Electro-optic tensor	$r_{33} = 333$ pm/V,	[15]
	$r_{42} = r_{51} = 38$ pm/V	[15]
Dielectric tensor	$\epsilon_{11} = \epsilon_{22} = 470$, $\epsilon_{33} = 880$	[16]
Thickness	$d = 4$ mm	
Electron-hole competition factor	$\bar{\sigma} = 1$	[17]
Modulation reduction	$R \approx 0.7$	
Effective trap density	$N_{\text{eff}} \approx 2 \times 10^{16}$ cm^{-3}	[18]

A. Process $\mathcal{A}$:(ee-ee)

For the computation of the output intensities of the process $\mathcal{A}$:(ee-ee) in SBN:Cr we use a pump angle (in air) of $\theta_p = 31°$ which corresponds to the experiment of [8]. The

TABLE II. Set of material-specific parameters needed for the computation of parametric scattering processes in the BCT:Rh sample used in [9].

Property	Value	Ref.
Material	$Ba_{0.77}Ca_{0.23}TiO_3$	
Doping	370 ppm Rh	
Symmetry group	4*mm*	
Refractive indices	$n_o = 2.456$, $n_e = 2.402$	[19]
	$r_{13} = r_{23} = 36$ pm/V,	[20]
Electro-optic tensor	$r_{33} = 140$ pm/V,	[20]
	$r_{42} = r_{51} = 190$ pm/V	[21]
Dielectric tensor	$\epsilon_{11} = \epsilon_{22} = 1120$, $\epsilon_{33} = 240$	[22]
Thickness	$d = 3.7$ mm	
Electron-hole competition factor	$\bar{\sigma} = -1$	[23]
Modulation reduction	$R \approx 0.5$	
Effective trap density	$N_{\text{eff}} = 3 \times 10^{16}$ cm^{-3}	[23]

TABLE III. Set of material-specific parameters needed for the computation of parametric scattering processes in a (typical) highly doped $LiNbO_3$:Fe crystal. The overall iron concentration is $c_{Fe} = 56 \times 10^{18}$ cm^{-3}. The ratio $c_{Fe^{2+}}/c_{Fe^{3+}} = 0.15$ is chosen to be similar to that of the sample used in [11].

Property	Value	Ref.
Material	$LiNbO_3$	
Doping	0.14 wt % Fe	
Symmetry group	$3m$	
Refractive indices	$n_o = 2.323$, $n_e = 2.234$	[24]
Electro-optic tensor	$r_{13} = r_{23} = 10.0$ pm/V,	[25]
	$r_{33} = 32.2$ pm/V,	[25]
	$r_{42} = r_{51} = 32.0$ pm/V,	[25]
	$r_{22} = -r_{12} = -2r_{61}$ = 6.8 pm/V	[25]
	$\beta_{311} = \beta_{322} = 21.9$ GV^{-1},	[26]
	$\beta_{333} = 21.9$ GV^{-1},	[26]
Photovoltaic tensor	$\beta_{131} = (1.3 - 13i)$ GV^{-1},	[27]
	$\beta_{222} = -\beta_{211} = -2\beta_{112}$ = 5.5 GV^{-1}	[26]
Dielectric tensor	$\epsilon_{11} = \epsilon_{22} = 85.1$, $\epsilon_{33} = 28.7$	[28]
Specific photoconductivity	$\alpha\chi = 8 \times 10^{-15}$ m/V^2	[29]
Thickness	$d = 1$ mm	
Electron-hole competition factor	$\bar{\sigma} = 1$	[30]
Modulation reduction	$R \approx 1$	[31]
Effective trap density	$N_{eff} \approx c_{Fe^{2+}}$ = 7.3×10^{18} cm^{-3}	[32]

pump waves have extraordinary light polarization. Furthermore, we chose $\Phi_\alpha^0 = \Phi_\beta^0 = 0$ and $\Phi_\gamma^0 = \Phi_\delta^0 = 0$ as the optimal phases of the pump waves α, β and the initial scattering waves γ, δ. Here we do not include frequency detunings ($\Omega = 0$): For crystals with a dominating diffusion charge transport (e.g., SBN and BCT) and in the absence of an external electric field these frequency detunings give usually no positive effect on the rate of spatial amplification. Figure 4 shows a photograph of the scattered light distribution on a screen behind the crystal. The corresponding computed image is displayed in Fig. 5.

The computed image is qualitatively in good agreement with the experimentally observed picture, including the characteristic contrast of the ring with respect to the scattering background. In the lower half plane of the Figs. 4 and 5 the ring is dark on the bright scattering background while in the upper half plane the contrast is inverse. Figure 6 shows the intensity on the ring versus the azimuth angle ϕ_δ. The 2WM contribution leads to strong positive (lower half plane) and negative (upper half plane) light amplification of the background. As Fig. 6 clarifies, the additional 4WM contribution on the ring reduces this asymmetric amplification drastically. This feature was already explained on the basis of exponential gain factors [33], where the overall exponential gain for the full ring has found to be zero. Nevertheless, as our results

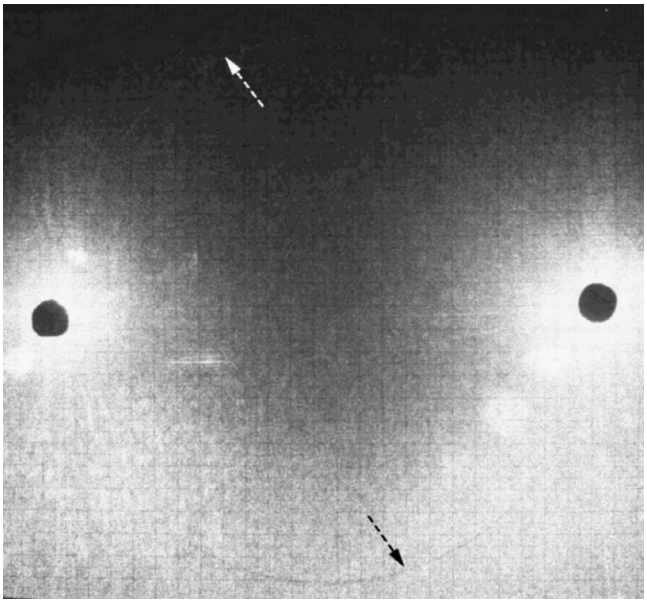

FIG. 4. Photograph of the scattering ring of the parametric process $\mathcal{A}$:(ee-ee) on a screen behind the SBN:Cr sample [8].

in Fig. 6 demonstrate, we have positive amplification of the initial scattering waves of the ring. This amplification stems only from the preexponential factors entering the steady-state amplitudes (5) and (6) of the scattering waves while the exponential terms do not contribute in this case. The observation of the bright half ring on the dark background (upper half plane of Fig. 4) is a proof that the preexponential terms can have a significant influence on the visibility of certain scattering patterns. Varying the strength of the initial scattering will not affect our results qualitatively.

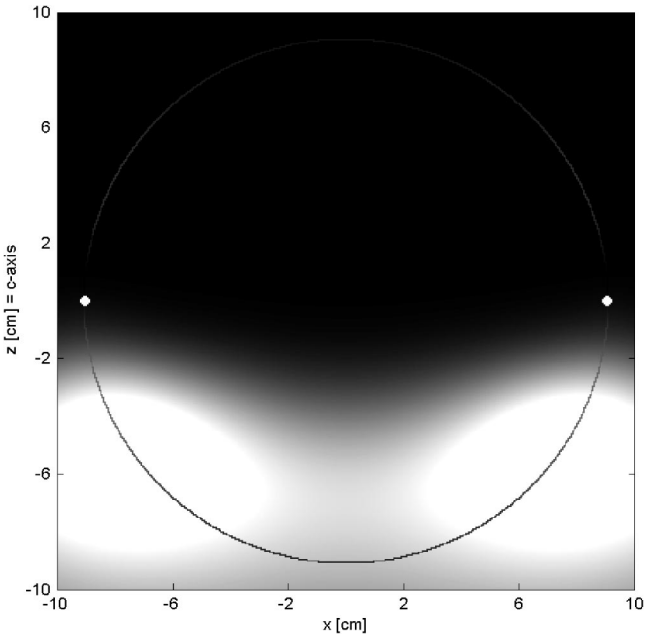

FIG. 5. Computed image of the parametric process $\mathcal{A}$:(ee-ee) on a screen in a typical distance of 10 cm behind the SBN:Cr sample. The image shows the isotropically scattered light of extraordinary polarization. The bright dots mark the pump beam spots.

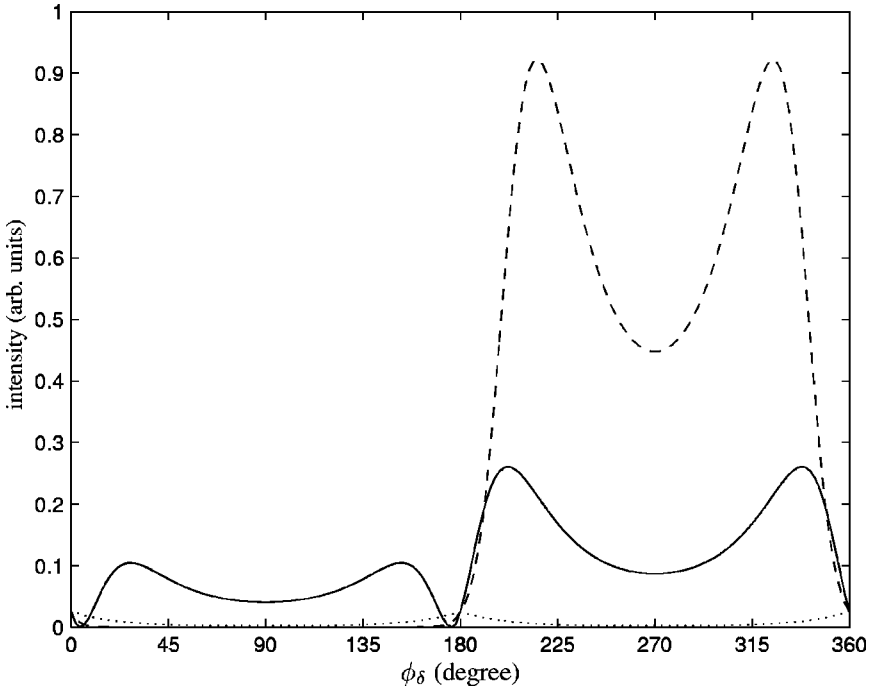

FIG. 6. Calculated intensity I_δ (in arbitrary units) of the scattering wave δ along the ring of the parametric process $\mathcal{A}$:(ee-ee) in the SBN:Cr sample. The solid line is the overall intensity $I_\delta^{\mathrm{2WM+4WM}}$ which contains both the 2WM and 4WM contributions. The dashed line corresponds to I_δ^{2WM} and includes only the 2WM contribution. Furthermore, the dotted line represents the initial scattering intensity. Here ϕ_δ starts counterclockwise from the right-hand pump beam spot ($\phi_\delta = 0°$).

B. Processes $\mathcal{A},\mathcal{B}$:(ee-oe)

In our computation of the output intensities of the processes $\mathcal{A},\mathcal{B}$:(ee-oe) in BCT:Rh we set the pump angle (in air) to $\theta_p = 17°$. Again, the pump beams have extraordinary light polarization. For the process $\mathcal{A}$:(ee-oe) we chose $\Phi_\alpha^0 = \Phi_\beta^0 = 0$ and $\Phi_\gamma^0 = \pi/2$, $\Phi_\delta^0 = 0$ as the optimal phases of the pump waves α,β and the initial scattering waves γ,δ. For the process $\mathcal{B}$:(ee-oe) these values are $\Phi_\alpha^0 = \Phi_\beta^0 = \Phi_\gamma^0 = \Phi_\delta^0 = 0$. We do not include frequency detunings for both processes in BCT because, again, they do not have a positive effect on the rate of spatial amplification. Figure 7 shows a photograph of the scattered light distribution (ordinary and extraordinary light polarization) on a screen behind the crystal. The picture includes the scattering patterns of the parametric processes $\mathcal{A}$:(ee-oe) (ring No. 5) and $\mathcal{B}$:(ee-oe) (line Nos. 1 and 2). Line Nos. 3 and 4 belong to the process $\mathcal{B}$:(ee-eo) which is symmetric to $\mathcal{B}$:(ee-oe). The corresponding computed image of these processes is displayed in Fig. 8.

The result of our calculation is qualitatively in good agreement with the experimental observation in Fig. 7. Especially the contrast of the dark lines (Nos. 2 and 3) is clearly reproduced in the computed image. Figure 9 shows a

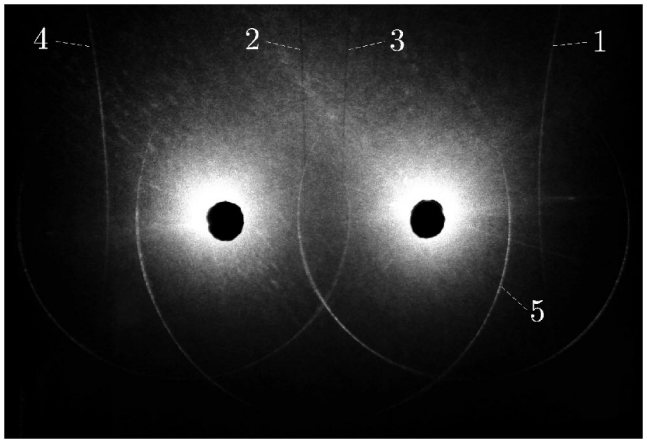

FIG. 7. Photograph of the scattering patterns which correspond to the parametric processes $\mathcal{A}$:(ee-oe) (ring No. 5) and $\mathcal{B}$:(ee-oe) (line Nos. 1 and 2) on a screen behind the BCT:Rh sample [9]. Line Nos. 3 and 4 belong to the process $\mathcal{B}$:(ee-eo) which is symmetric to $\mathcal{B}$:(ee-oe).

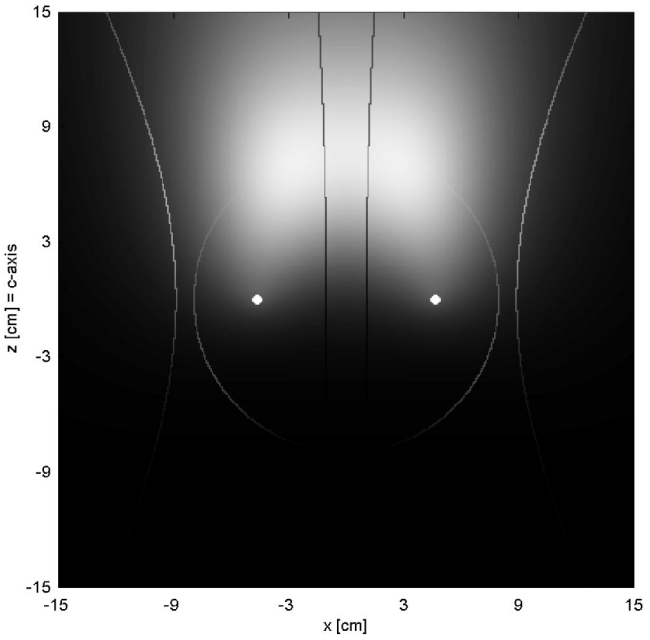

FIG. 8. Computed image of the parametric processes $\mathcal{A}$:(ee-oe) (ring) and $\mathcal{B}$:(ee-oe,eo) (lines) on a screen 10 cm behind the BCT:Rh sample. The image shows both, the isotropically and anisotropically scattered light. The bright dots again mark the pump beam spots.

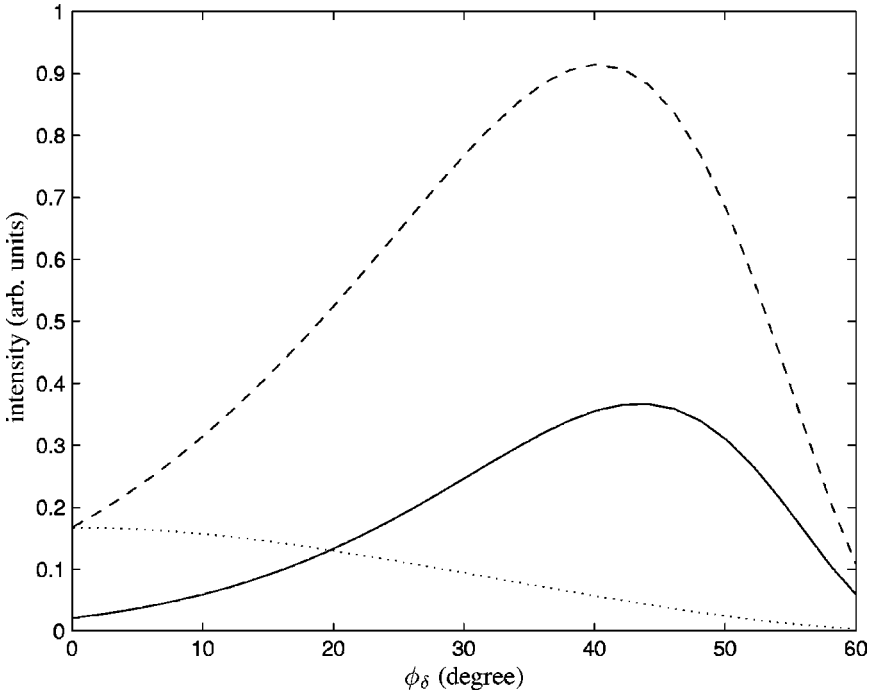

FIG. 9. Calculated intensity I_δ (in arbitrary units) of the scattering wave δ along the dark line of the parametric process $\mathcal{B}$:(ee-oe) in the BCT:Rh sample. The solid line is the overall intensity $I_\delta^{\mathrm{2WM+4WM}}$ which contains both the 2WM and 4WM contributions. The dashed line corresponds to I_δ^{2WM} and includes only the 2WM contribution. Furthermore, the dotted line represents the initial scattering intensity. Here ϕ_δ starts in the plane passing through the two pump beam spots ($\phi_\delta = 0°$) moving along the left-hand dark line to the border ($\phi_\delta \approx 60°$) of the image in Fig. 8.

detailed plot of the calculated intensity of the dark line (No. 2) corresponding to the extraordinarily polarized scattering wave of the parametric process $\mathcal{B}$:(ee-oe). This line as well as the surrounding scattering background are amplified due to the 2WM contribution. This amplification increases for larger grating vectors until space-charge-field-limiting effects occur. The amplification of the line, however, is also effected by the additional 4WM contribution. Here the 4WM part is based on the coupling between the two scattering waves of the process $\mathcal{B}$:(ee-oe) via the fundamental grating recorded by the pump waves. As a result, the ordinarily polarized scattering wave (corresponding bright line No. 1) is amplified at the expense of the extraordinarily polarized scattering wave, which thus becomes visible as a dark line on the bright scattering background. Again, the dark pattern originates from counteracting energy transfer processes (4WM against 2WM).

Finally we want to consider a special case of the parametric process $\mathcal{A}$:(ee-oe) where the two pump beams coincide at a pump angle $\theta_p = 0°$. In this geometry the process is also known as the inner scattering cone (ring) from experiments with only one pump beam [10–12]. Our computation is performed for the material $LiNbO_3$:Fe. Here we take into account frequency-detuned scattering waves as introduced in Sec. IV C with a frequency shift Ω satisfying the condition $\Omega t_d = 1$. In $LiNbO_3$ frequency detunings can lead to shifted gratings recorded via the photovoltaic charge transport and thus have a considerable influence on the two-beam coupling gain and the steady-state light amplification [34].

The result of our calculation is shown in Fig. 10. The computed image of the scattered light distribution includes both the ordinarily and extraordinarily polarized light. In contrast, Fig. 11 presents only the (weak) anisotropic (ordinarily polarized) part of the scattered light intensity scaled up by a factor of 10 compared to Fig. 10. The image of the anisotropic scattering ring is qualitatively in good agreement with experimental observations. This ring, however, is too weak to be visible on the bright isotropic scattering background in the complete image of Fig. 10. Instead we observe a dark ring which corresponds to the extraordinarily polarized scattering wave (isotropic light) of the process $\mathcal{A}$:(ee-oe). As Fig. 12 clarifies, it is the result of true four-wave mixing [via the nondiagonal elements of the interaction matrix (8a)] with an energy transfer direction opposite to the two-wave mixing part. Thus the overall intensity (2WM

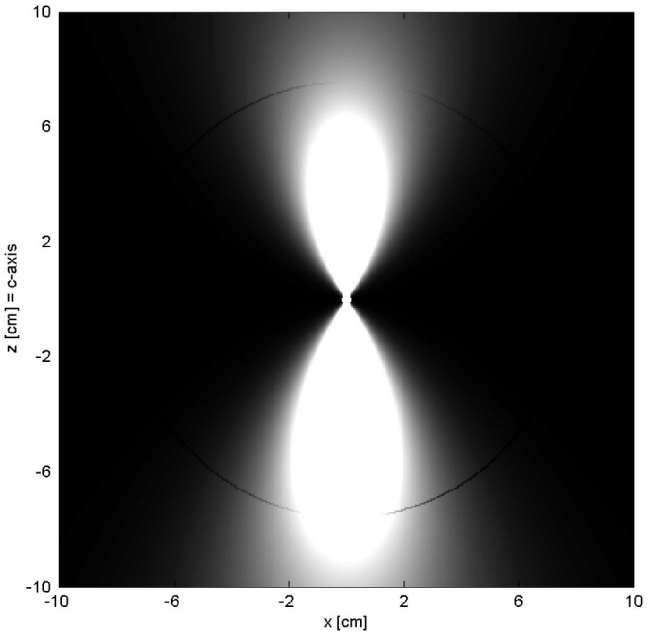

FIG. 10. Computed image of the parametric process $\mathcal{A}$:(ee-oe) (ring) on a screen 10 cm behind the $LiNbO_3$:Fe crystal. The image shows both the isotropically and anisotropically scattered light. The spot of the pump beams is located in the center of the image.

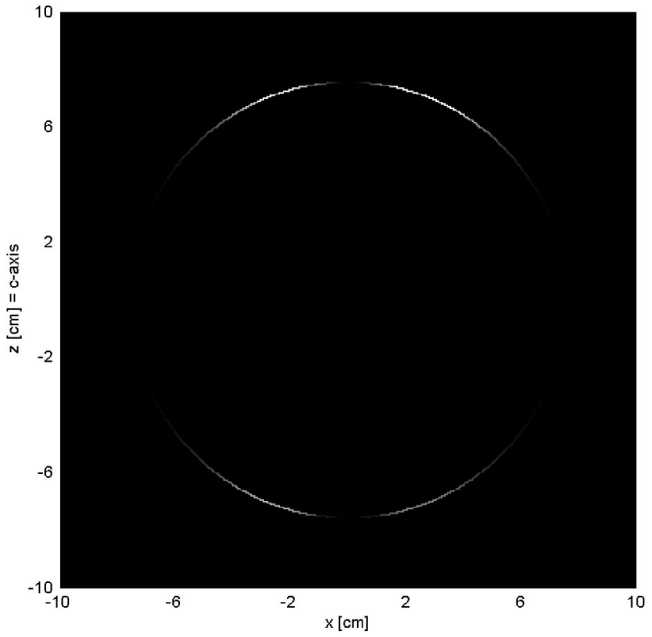

FIG. 11. Computed image of the parametric process $\mathcal{A}$:(ee-oe) (ring) on a screen 10 cm behind the $LiNbO_3$:Fe crystal. The image shows only the anisotropically scattered light.

+4WM) of the extraordinarily polarized scattering wave is lower than for the corresponding background (only 2WM). In this parametric process, the 4WM contribution requires anisotropic recording of gratings between the waves of the (weak) ordinarily polarized scattering ring (Fig. 11) and the pump wave(s) of extraordinary light polarization. This is achieved via spatially oscillating photovoltaic currents. The dark ring in Fig. 10 has been observed experimentally for specific $LiNbO_3$:Fe samples used by Rupp and Drees [11] already in 1986, but no explanation of this feature has been given. For the $LiNbO_3$:Fe crystal used in [35], however, no indications for parametric 4WM contributions to the recording mechanism of this process (e.g., no dark ring) could be found. Probably the iron doping and the associated photovoltaic charge transport of this sample are too weak.

We have performed the computation of the output intensities of the process $\mathcal{A}$:(ee-oe) also for initial material parameters of a typical copper-doped $LiNbO_3$ crystal. One major difference with respect to the energy transfer in iron-doped crystals is the change in the sign of β^a [27]. Nevertheless, the computed scattered light distribution we obtained is similar to that for the iron-doped crystal (Fig. 10). Therefore, we expect the dark ring to appear also for $LiNbO_3$:Cu crystals with sufficiently high doping.

We want to point out that the dark scattering patterns shown in the present work can be explained within our restriction of exact phase matching. In practice, however, scattering patterns with strong light amplification are sometimes accompanied by dark scattering patterns (e.g., dark rings) which correspond to small angular deviations from the directions of exact phase matching. For these angular deviations the scattered waves can still have considerably strong intensities while the phase of the waves can undergo strong variations. This kind of dark scattering patterns cannot be treated within our theoretical approach which is restricted only to the case of exact phase matching.

VI. SUMMARY AND OUTLOOK

Based on the model for parametric four-wave mixing processes in photorefractive media [5], we have performed computations of scattered light distributions corresponding to the parametric processes $\mathcal{A}$:(ee-ee) in SBN:Cr, $\mathcal{A},\mathcal{B}$:(ee-oe) in BCT:Rh and $\mathcal{A}$:(ee-oe) in $LiNbO_3$:Fe. Our computed images are qualitatively in good agreement with photographs of

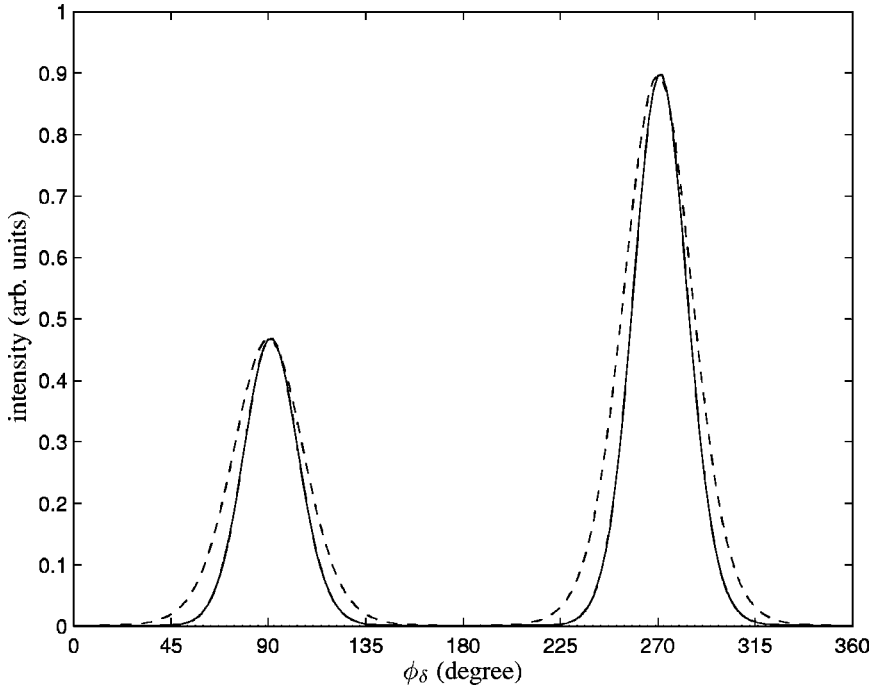

FIG. 12. Calculated intensity I_δ (in arbitrary units) of the scattering wave δ along the dark ring of the parametric process $\mathcal{A}$:(ee-oe) in the $LiNbO_3$:Fe sample. The solid line is the overall intensity $I_\delta^{2WM+4WM}$ which contains both the 2WM and 4WM contributions. The dashed line corresponds to I_δ^{2WM} and includes only the 2WM contribution. Here ϕ_δ starts counterclockwise from the right-hand intersection point (ϕ_δ=0°) of the ring with horizontal plane passing through the pump beam spot in Fig. 12.

the experimentally observed light patterns. Especially the contrast of the dark scattering patterns can be rebuild theoretically. Our calculations reveal that these dark patterns result from counteracting energy transfer mechanisms (two-wave mixing versus true four-wave mixing). The computer application which has been developed in the framework of the present work provides the opportunity to study the influence of numerous material properties and experimental conditions. In general, the computation also allows for a quantitative analysis of scattered light intensities. This is, however, difficult to realize since exact values for all material-specific parameters have to be found. In addition, we have to learn more about the seed scattering (initial phases, amplitudes, and detuned frequencies) whose nature is up to now mostly unknown.

ACKNOWLEDGMENT

Valuable help by E. Krätzig is gratefully acknowledged.

[1] R. Magnusson and T. K. Gaylord, Appl. Opt. **13**, 1545 (1974).
[2] J. J. Amodei and D. L. Staebler, J. Appl. Phys. **43**, 1042 (1972).
[3] A. Yariv and D. Pepper, Opt. Lett. **1**, 16 (1977).
[4] M. Cronin-Golomb, B. Fisher, J. White, and A. Yariv, IEEE J. Quantum Electron. **QE-20**, 12 (1984).
[5] B. I. Sturman, S. G. Odoulov, and M. Y. Goulkov, Phys. Rep. **275**, 197 (1996).
[6] A. A. Zozulya, M. Saffman, and D. Z. Anderson, Phys. Rev. Lett. **73**, 818 (1994).
[7] A. A. Zozulya and D. Z. Anderson, Phys. Rev. A **51**, 1520 (1995).
[8] S. Schwalenberg and E. Krätzig, Appl. Phys. B: Lasers Opt. **77**, 37 (2003).
[9] S. Schwalenberg and E. Krätzig, J. Opt. A, Pure Appl. Opt. **6**, 349 (2004).
[10] M. D. Ewbank, P. Yeh, and J. Feinberg, Opt. Commun. **59**, 423 (1986).
[11] R. A. Rupp and F. W. Drees, Appl. Phys. B: Photophys. Laser Chem. **39**, 223 (1986).
[12] D. A. Temple and C. Warde, J. Opt. Soc. Am. B **3**, 337 (1986).
[13] M. Y. Goulkov, T. Granzow, U. Dörfler, T. Woike, M. Imlau, and R. Pankrath, Appl. Phys. B: Lasers Opt. **76**, 407 (2004).
[14] D. Kip, S. Aulkemeyer, K. Buse, F. Mersch, R. Pankrath, and E. Krätzig, Phys. Status Solidi A **154**, K5 (1996).
[15] U. B. Dörfler, R. Piechatzek, T. Woike, M. K. Imlau, V. Wirth, L. Bohatý, T. Volk, R. Pankrath, and M. Wöhlecke, Appl. Phys. B: Lasers Opt. **68**, 843 (1999).
[16] R. R. Neurgaonkar and L. E. Cross, Mater. Res. Bull. **21**, 893 (1986).
[17] M. D. Ewbank, R. R. Neurgaonkar, W. K. Cory, and J. Feinberg, J. Appl. Phys. **62**, 374 (1987).
[18] Y. Tomita and A. Suzuki, Appl. Phys. A: Solids Surf. **59**, 579 (1994).
[19] M. Simon, F. Mersch, C. Kuper, S. Mendricks, S. Wevering, J. Imbrock, and E. Krätzig, Phys. Status Solidi A **159**, 559 (1997).
[20] C. Kuper, K. Buse, U. van Stevendaal, M. Weber, T. Leidlo, H. Hesse, and E. Krätzig, Ferroelectrics **208-209**, 213 (1996).
[21] J. Neumann, M. Röwe, H. Veenhuis, R. Pankrath, and E. Krätzig, Phys. Status Solidi B **215**, R9 (1999).
[22] C. Kuper, R. Pankrath, and H. Hesse, Appl. Phys. A: Mater. Sci. Process. **65**, 301 (1997).
[23] H. Veenhuis, T. Börger, K. Peithmann, M. Flaspöhler, K. Buse, R. Pankrath, H. Hesse, and E. Krätzig, Appl. Phys. B: Lasers Opt. **70**, 797 (2000).
[24] D. S. Smith, H. D. Riccius, and R. P. Edwin, Opt. Commun. **17**, 332 (1976).
[25] I. P. Kaminow and E. H. Turner, *Handbook of Lasers* (Chemical Rubber Publishing, Cleveland, OH, 1971), Chap. 15, pp. 447–459.
[26] H. G. Festl, P. Hertel, E. Krätzig, and R. von Baltz, Phys. Status Solidi B **113**, 157 (1982).
[27] S. G. Odoulov, Ferroelectrics **91**, 213 (1989).
[28] R. T. Smith and F. S. Welsh, J. Appl. Phys. **42**, 2219 (1971).
[29] K. Peithmann, A. Wiebrock, and K. Buse, Appl. Phys. B: Lasers Opt. **68**, 777 (1999).
[30] R. Orlowski and E. Krätzig, Solid State Commun. **27**, 1351 (1978).
[31] U. van Stevendaal, K. Buse, H. Malz, H. Veenhuis, and E. Krätzig, J. Opt. Soc. Am. B **15**, 2868 (1998).
[32] I. Nee, M. Müller, K. Buse, and E. Krätzig, J. Appl. Phys. **88**, 4282 (2000).
[33] S. Schwalenberg and E. Krätzig, Appl. Phys. B: Lasers Opt. **79**, 423 (2004).
[34] M. Goulkov, S. Odoulov, T. Woike, J. Imbrock, M. Imlau, E. Krätzig, C. Bäumer, and H. Hesse, Phys. Rev. B **65**, 195111 (2002).
[35] S. Schwalenberg, F. Rahe, and E. Krätzig, Opt. Commun. **209**, 467 (2002).